Journal of the Korean Astronomical Society
53: 161 ∼ 168, 2020 December
https://doi.org/10.5303/JKAS.2020.53.6.161
pISSN: 1225-4614 · eISSN: 2288-890X
http://jkas.kas.org
Published under Creative Commons license CC BY-SA 4.0

OGLE-2017-BLG-1049: Another Giant Planet Microlensing Event

Yun Hak Kim [1,2], Sun-Ju Chung [1,2,28], A. Udalski [5,29], Ian A. Bond [7,30], Youn Kil Jung [1,28], Andrew Gould [1,3,4,28], Michael D. Albrow [8,28], Cheongho Han[9,28], Kyu-Ha Hwang[1,28], Yoon-Hyun Ryu[1,28], In-Gu Shin[1,28], Yossi Shvartzvald [10,28], Jennifer C. Yee [11,28], Weicheng Zang [12,28], Sang-Mok Cha [1,13,28], Dong-Jin Kim [1,28], Hyoun-Woo Kim [1,27,28], Seung-Lee Kim [1,2,28], Chung-Uk Lee [1,2,28], Dong-Joo Lee [1,28], Yongseok Lee [1,13,28], Byeong-Gon Park [1,2,28], Richard W. Pogge [3,28], Radek Poleski [5,29], Przemek Mróz [6,29], Jan Skowron [5,29], Michal K. Szymański [5,29], Igor Soszyński [5,29], Pawel Pietrukowicz [5,29], Syzmon Kozłowski [5,29], Krzysztof Ulaczyk [5,14,29], Krzysztof A. Rybicki [5,29], Patryk Iwanek [5,29], Fumio Abe [15,30], Richard Barry [16,30], David P. Bennett [16,17,30], Aparna Bhattacharya [16,17,30], Martin Donachie [18,30], Hirosane Fujii [21,30], Akihiko Fukui [19,20,30], Yoshitaka Itow [15,30], Yuki Hirao [21,30], Rintaro Kirikawa [21,30], Iona Kondo [21,30], Naoki Koshimoto [22,23,30], Yutaka Matsubara [15,30], Yasushi Muraki [15,30], Shota Miyazaki [21,30], Clément Ranc [16,30], Nicholas J. Rattenbury [18,30], Yuki Satoh [21,30], Hikaru Shoji [21,30], Takahiro Sumi [21,30], Daisuke Suzuki [21,30], Paul J. Tristram [25,30], Yuzuru Tanaka [21,30], Tsubasa Yamawaki [21,30], and Atsunori Yonehara [26,30]

[1]Korea Astronomy and Space Science Institute, 776 Daedeokdae-ro, Yuseong-Gu, Daejeon 34055, Korea; sherlock@kasi.re.kr
[2]University of Science and Technology, Korea, (UST), 217 Gajeong-ro, Yuseong-gu, Daejeon 34113, Korea
[3]Department of Astronomy, Ohio State University, 140 W. 18th Ave., Columbus, OH 43210, USA
[4]Max-Planck-Institute for Astronomy, Königstuhl 17, 69117 Heidelberg, Germany
[5]Warsaw University Observatory, AI. Ujazdowskie 4, 00-478 Warszawa, Poland
[6]Division of physics, Mathematics, and Astronomy, California institute of Technology, Pasadena, CA 91125, USA
[7]Institute of Natural and Mathematical Science, Massey University, Auckland 0745, New Zealand
[8]Department of Physics and Astronomy, University of Canterbury, Private Bag 4800 Christchurch, New Zealand
[9]Department of Physics, Chungbuk National University, Cheongju 28644, Korea
[10]Department of Particle Physics and Astrophysics, Weizmann Institute of Science, Rehovot 76100, Israel
[11]Center for Astrophysics — Harvard & Smithsonian, 60 Garden St., Cambridge, MA 02138, USA
[12]Department of Astronomy and Tsinghua Centre for Astrophysics, Tsinghua University, Beijing 100084, China
[13]School of Space Research, Kyung Hee University, Giheung-gu, Yongin, Gyeonggi-do, 17104, Korea
[14]Department of Physics, University of Warwick, Gibbet Hill Road, Coventry, CV4 7AL, UK
[15]Institute for Space-Earth Environmental Research, Nagoya University, Nagoya 464-8601, Japan
[16]Code 667, NASA Goddard Space Flight Center, Greenbelt, MD 20771, USA
[17]Department of Astronomy, University of Maryland, College Park, MD 20742, USA
[18]Department of Physics, University of Auckland, Private Bag 92019, Auckland, New Zealand
[19]Department of Earth and Planetary Science, Graduate School of Science, The University of Tokyo, 7-3-1 Hongo, Bunkyo-ku, Tokyo 113-0033, Japan
[20]Instituto de Astrofísica de Canarias, Vía Láctea s/n, E-38205 La Laguna, Tenerife, Spain
[21]Department of Earth and Space Science, Graduate School of Science, Osaka University, Toyonaka, Osaka 560-0043, Japan
[22]Department of Astronomy, Graduate School of Science, The University of Tokyo, 7-3-1 Hongo, Bunkyo-ku, Tokyo 113-0033, Japan
[23]National Astronomical Observatory of Japan, 2-21-1 Osawa, Mitaka, Tokyo 181-8588, Japan
[24]School of Chemical and Physical Science, Victoria University, Wellington, New Zealand
[25]University of Canterbury Mt. John Observatory, P.O. Box 56, Lake Tekapo 8770, New Zealand
[26]Department of Physics, Faculty of Science, Kyoto Sangyo University, Kyoto 603-8555, Japan
[27]Department of Astronomy and Space Science, Chungbuk National University, Cheongju 28644, Republic of Korea
[28]The KMTNet Collaboration
[29]The OGLE Collaboration
[30]The MOA Collaboration

Received September 1, 2020; accepted December 1, 2020

Abstract: We report the discovery of a giant exoplanet in the microlensing event OGLE-2017-BLG-1049, with a planet–host star mass ratio of $q = 9.53 \pm 0.39 \times 10^{-3}$ and a caustic crossing feature in Korea Microlensing Telescope Network (KMTNet) observations. The caustic crossing feature yields an angular Einstein radius of $\theta_{\rm E} = 0.52 \pm 0.11$ mas. However, the microlens parallax is not measured because the time scale of the event, $t_{\rm E} \simeq 29$ days, is too short. Thus, we perform a Bayesian analysis to estimate physical quantities of the lens system. We find that the lens system has a star with mass $M_{\rm h} = 0.55^{+0.36}_{-0.29}\ M_\odot$ hosting a giant planet with $M_{\rm p} = 5.53^{+3.62}_{-2.87}\ M_{\rm Jup}$, at a distance of $D_{\rm L} = 5.67^{+1.11}_{-1.52}$ kpc. The projected star–planet separation is $a_\perp = 3.92^{+1.10}_{-1.32}$ au. This means that the planet is located beyond the snow line of the host. The relative lens–source proper motion is $\mu_{\rm rel} \sim 7$ mas yr^{-1}, thus the lens and source will be separated from each other within 10 years. After this, it will be possible to measure the flux of the host star with 30 meter class telescopes and to determine its mass.

Key words: gravitational lensing: micro

1. INTRODUCTION

Up to now, 4301 exoplanets (as of 2020 November 5)[1] have been detected using various methods including radial velocity, transit, direct imaging, and microlensing observations. Over 90% of them have been discovered with the radial velocity and transit methods, and they are almost all located close to their host stars, i.e., hot planets. By contrast, almost all of the exoplanets discovered by microlensing are cold planets, which lie at or beyond the snow line where the water can form ice grains in the proto-planetary disk (Kennedy & Kenyon 2008).

The majority of host stars of microlensing exoplanets are faint low-mass M dwarf stars, which are generally difficult to detect with radial-velocity and transit observations. This is because microlensing does not depend on the brightness of objects, only on the mass (Gaudi 2012). The microlensing host stars have many giant planets beyond the snow line, suggesting that giant planets around M dwarfs might be common (e.g., Gould et al. 2006; Sumi et al. 2010; Montet et al. 2014). This is contrary to the prediction by the core-accretion model of planet formation according to which planets around M dwarf should be rare (Ida & Lin 2004; Laughlin et al. 2004; Kennedy et al. 2006), while it is consistent with the prediction by the disk instability model according to which they are common (Boss 2006). These results imply that microlensing exoplanets are very important for the understanding of planet formation.

As of now, the total number of exoplanets detected by microlensing has reached 105 (as of 2020 November 5),[1] which is small compared to the numbers detected by the radial velocity and transit methods. Of these, 42% of the host stars have masses that are only estimated by a Bayesian analysis, which investigates the probability distributions of physical parameters (Jung et al. 2018). Since M dwarfs are the most common stars in the Galaxy, this necessarily results in a prediction that most of the host stars are M dwarfs. At the same time, the Bayesian prior explicitly assumes that planet frequency is independent of host star mass.

In order to truly test planet formation theory, we need to assemble a sample of microlensing giant planets whose host stars have direct mass measurements. Often, such measurements can be made by resolving the light from the lens star using high-resolution imaging. For example, Dong et al. (2009) showed that the giant planet in OGLE-2005-BLG-071 does indeed orbit an M-dwarf, a result that was later confirmed by Bennett et al. (2020). By contrast, Vandorou et al. (2020) measured the lens flux for MOA-2013-BLG-220, which shows a clear difference from the central value of the Bayesian analysis. Robust flux measurements are best made after the source and the lens have separated (Battacharya et al. 2017), i.e. many years after the time of the event. Thus, the first step to a statistical study of giant planets around M dwarfs is to identify a large sample of giant planets for future high-resolution follow-up observations.

Until now, 54 planetary systems composed of giant planets around M dwarf have been detected by microlensing. The microlensing event OGLE-2017-BLG-1049 is such the planetary system. In this paper, we report the analysis of the planetary event OGLE-2017-BLG-1049. The light curve of the event has a U-shaped caustic crossing feature. This feature occurs when the source crosses the caustic, which represents the set of source positions at which a magnification of a point source becomes infinite (Chung et al. 2005, Han 2005). The caustic crossing feature was covered by the Korea Microlensing Telescope Network (KMTNet; Kim et al. 2016).

The paper is organized as follows. Observations of the event are described in Section 2. In Section 3, the light curve analysis is described, and the physical parameters of the lens are estimated in Section 4. We summarize our results in Section 5.

2. OBSERVATIONS

The microlensing event OGLE-2017-BLG-1049 was discovered on 2017 June 4 by the Optical Gravitational Lensing Experiment (OGLE; Udalski 2003) survey with the 1.3 meter Warsaw telescope at Las Campanas Observatory in Chile. The equatorial and galactic coordinates of the event are $(\alpha, \delta) = (17^{\rm h}58^{\rm m}8.05^{\rm s}, -27°08'39.20'')$ and $(l, b) = (2.950°, -1.461°)$, respectively.

The event was also found by the KMTNet post-season event finder (Kim et al. 2018) and was designated KMT-2017-BLG-0370. KMTNet observations were conducted using three identical telescopes at the Cerro Tololo Inter-American Observatory in Chile (KMTC), South African Astronomical Observatory in South Africa (KMTS), and Siding Spring Observatory in Australia (KMTA). The event lies in two overlapping fields, BLG03 and BLG43, with a combined cadence of $\Gamma = 4$ hr^{-1}. The majority of images were taken in I band, some images were taken in V band to measure the color of the source star. The KMTNet data were reduced with the `pySIS` pipeline based on Difference Image Analysis (DIA; Alard & Lupton 1998, Albrow et al. 2009). The event was originally analyzed using OGLE and KMT data because it had not been noted by the Microlensing Observations in Astrophysics (MOA; Sumi et al. 2016). The best-fit model without MOA predicts the second strong anomaly feature at the time of a data gap, which might be regarded as "suspicious" (see Figure 1). A review of the MOA observations showed that they had observed this field during the gap time, so a special data reduction was carried out. The MOA data were included to confirm the second anomaly feature in the gap (see Figure 2).

In general, each observatory has their own photometry pipeline packages and they typically underestimate the true error due to their systematics (Yee et al. 2012). Hence, the photometric errors for each data set in magnitude need to be normalized before modeling the data together. We renormalize the error bars for all data sets except OGLE. For OGLE data sets, Skowron et al. (2016) already did the renormalization for all their

CORRESPONDING AUTHOR: S.-J. Chung (sjchung@kasi.re.kr)
[1] https://exoplanetarchive.ipac.caltech.edu/index.html

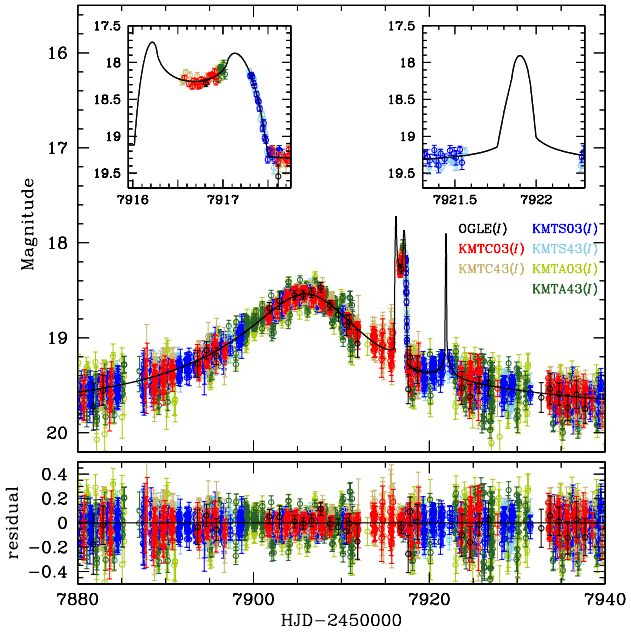

Figure 1. Best-fit light curve (black continuous line) of OGLE-2017-BLG-1049 without MOA data. Data sets from different observatories are displayed in different colors. The best-fit parameters for this case are given in the first column of Table 2.

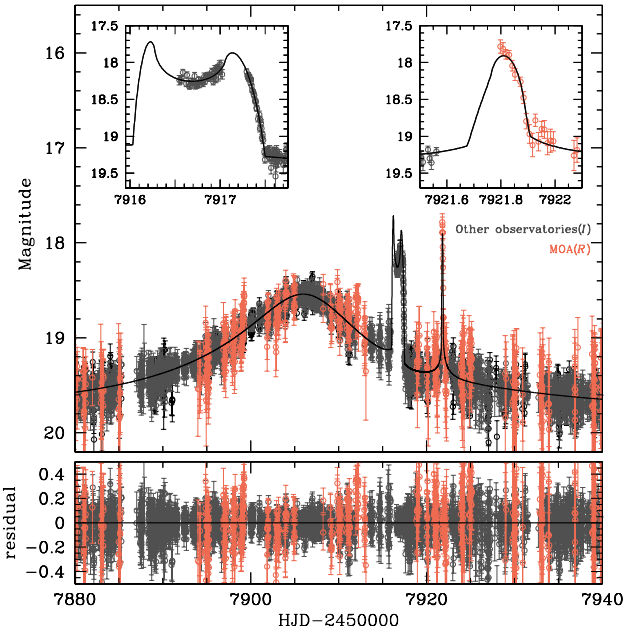

Figure 2. Best-fit light curve of OGLE-2017-BLG-1049 including MOA data (black continuous line). MOA data are colored red, all other data are colored gray. The best-fit parameters for this case are given in the second column of Table 2.

survey fields, and thus they provide the error correction coefficients. From this, we adopt the rescaling parameters for OGLE. For the renormalization, we follow the procedure described in Yee et al. (2012),

$$\sigma' = k\sqrt{\sigma_i^2 + (\sigma_0)^2}, \quad (1)$$

where σ_i is the original error bar of the ith data point, and k and σ_0 are the rescaling parameters required to achieve $\chi^2/\mathrm{dof} = 1$. The rescaling parameters are presented in Table 1.

3. Light Curve Analysis

The KMTNet data show a clear short-duration caustic crossing feature around HJD$' \sim 7917$, as shown in Figure 1. This implies that the lens is likely a binary system having a low-mass companion (Gould 2000, 2001; Gaudi 2012). Thus, we conduct standard binary lens modeling, which requires seven parameters including three single lens parameters (t_0, u_0, t_E), three binary lens parameters (s, q, α), and ρ. Here t_0 is the time of the closest source approach to the lens, u_0 is the separation between the source and the lens at t_0 which is normalized by the angular Einstein ring radius (θ_E), which corresponds to the total lens mass, t_E is the time duration of crossing θ_E, s is the projected separation between the lens components in units of θ_E, q is the mass ratio of the lens components, $q = m_2/m_1$, in which m_1 and m_2 are the masses of the host and its companion, respectively, α is the angle between the source trajectory and the binary axis, and $\rho = \theta_*/\theta_\mathrm{E}$ is the normalized source radius, where θ_* is the angular size of the source star. In addition to the geometric parameters, there are two flux parameters for each observatory, the source flux f_s and the blended flux f_b. At a given time t, the observed flux $F(\mathrm{t})$ is

$$F(t) = f_\mathrm{s} A(t) + f_\mathrm{b}, \quad (2)$$

where $A(t)$ is the magnification as a function of time.

We carry out a grid search on three parameters $(\log s, \log q, \alpha)$ for local χ^2 minima using a Markov chain Monte Carlo (MCMC) algorithm. We investigate the parameter ranges $-1 \leqslant \log s \leqslant 1$, $-4.0 \leqslant \log q \leqslant 0$ and, $0 \leqslant \alpha \leqslant 2\pi$, with 100, 100, and 21 uniform grid steps, respectively. In the grid search, $\log(s, q)$ are fixed, while the remaining parameters are allowed to vary in the chain. From the local grid search, we found four possible local χ^2 minima at $(s, q) = (1.32, 9.0\times10^{-3}), (1.20, 1.0\times10^{-3}), (0.81, 1.5\times10^{-2})$, and $(0.78, 4.4\times10^{-2})$. We then seed these four sets of local solutions into the MCMC for which all parameters are allowed to vary. During the MCMC, the two close solutions converge to $(s, q) = (0.80, 2.22\times10^{-2})$, while the two wide solutions converge to $(s, q) = (1.32, 9.53\times10^{-3})$. However, the χ^2 of the final close solution is much larger than the one of the final wide solution, by a factor ~ 1570. Eventually, this event has only one wide solution.

Figure 2 shows the best-fit light curve of OGLE-2017-BLG-1049. The best-fit lensing parameters are presented in Table 2. As can be seen from Figures 1 and 2, the two major perturbations to the light curve were caused by the resonant caustic (Erdl & Schneider 1993, Gaudi 2012), which is induced by $(s, q) = (1.32,\ 9.53\times$

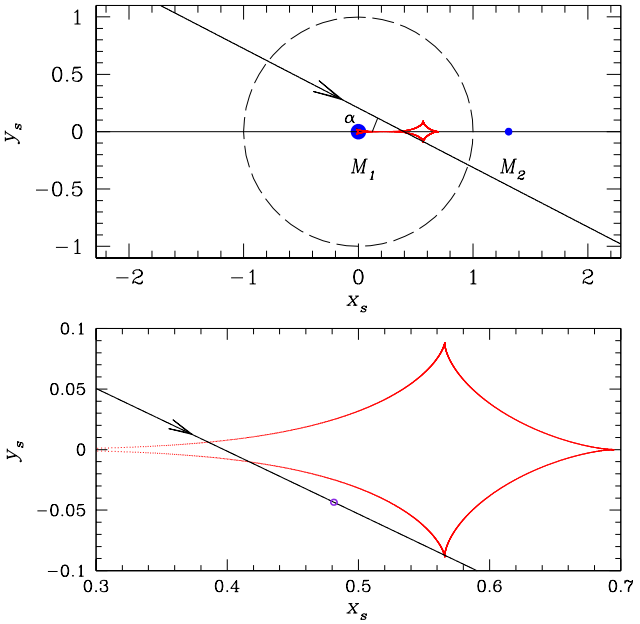

Figure 3. Geometry of the best-fit model including MOA data. The corresponding lensing parameters are given in the second column of Table 2. The coordinates (x_s, y_s) are normalized by the angular Einstein radius corresponding to the total mass of the lens. The black dashed and solid lines in the upper panel indicate the angular Einstein ring and the source star trajectory, respectively, while α is the angle between the source trajectory and the binary axis. The caustics are plotted in red. M_1 and M_2 are the host and planetary companion, respectively. The lower panel AI a zoom-in on the caustic and cusp crossing regions. The purple open circle indicates the normalized source size.

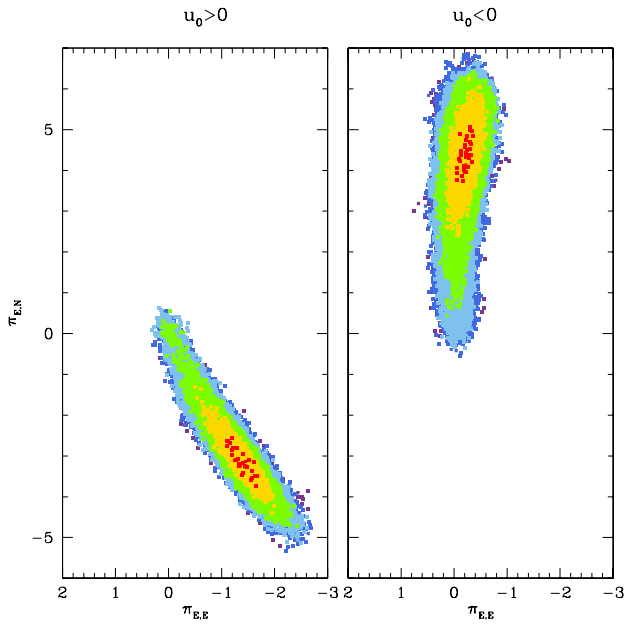

Figure 4. $\Delta\chi^2$ distribution of $(\pi_{E,E}, \pi_{E,N})$ for two best-fit parallax+orbital models, $u_0 > 0$ and $u_0 < 0$. The colors of red, yellow, green, light blue, blue, and purple represent regions with $\Delta\chi^2 < 1, 4, 9, 16, 25$ and 36 from the best-fit value, respectively.

10^{-3}), and its geometry is shown in Figure 3. We initially perform the MCMC modeling with OGLE and KMTNet data only. As a result, the first perturbation at HJD$' \sim$ 7917 was caused by a caustic crossing and was well covered by KMT data, whereas the second perturbation around HJD$' \sim 7922$ was caused by a cusp crossing, but unfortunately, due to the gap in the data, the second perturbation looks doubtful (see Figure 1), even though the first perturbation was well fitted.

However, after reviewing the MOA data base, it was determined that MOA had observed this event during the data gap, although they did not alert this event. We repeated our MCMC modeling, now including the MOA data set. We find that the two modeling results with and without the MOA data agree at the 1σ level (see Table 2). The best-fit light curve from modeling with the MOA data confirms that the second perturbation is real, even though there are some correlated residuals at the beginning of the night.

We additionally conduct binary lens modeling with high-order parameters including the microlens parallax (Gould 1992, 1994) and orbital motion (Dominik 1998). In microlensing, the parallax effect is caused by the Earth's orbital motion during the course of the event. The parallax is a vector with components parallel and perpendicular to the Earth's projected acceleration at the peak of the event; these are defined as $\pi_E = (\pi_{E,N}, \pi_{E,E})$ (Gould et al. 1994, Udalski et al. 2018). The orbital motion effect is caused by the orbital motion of the binary lens under the assumption of a linear orbital motion. It is described by two parameters, $(ds/dt, d\alpha/dt)$, which are the change rates of the binary separation and the orientation angle of the binary axis, respectively. However, the orbital motion effect can mimic the parallax effect (Batista et al. 2011, Skowron et al. 2011, Han et al. 2016). Hence, we model the event with both effects. We find that the best-fit parallax+orbital model, i.e. the case $u_0 > 0$, improves the fit by only $\Delta\chi^2 \lesssim 5$ compared to the standard model. This means that the high-order effects were not detected. Figure 4 shows that the magnitude of the microlens parallax is not well constrained, but its direction is. Therefore, we perform a Bayesian analysis to determine the physical parameters of the lens system, which will be described in Section 4.

4. PHYSICAL PARAMETERS

4.1. Angular Einstein radius

Thanks to the detection of the caustic crossing feature, we were able to measure the normalized source radius, $\rho = \theta_*/\theta_E$, from the model light curve. In order to determine the angular Einstein radius θ_E, we measure the source radius θ_* from the intrinsic brightness and color of the source star. As described in Yoo et al. (2004), the intrinsic brightness and color of the source can be determined from the offset between the red giant clump centroid (RGC) and the source in the instrumental color–magnitude diagram (CMD) under the assumption that

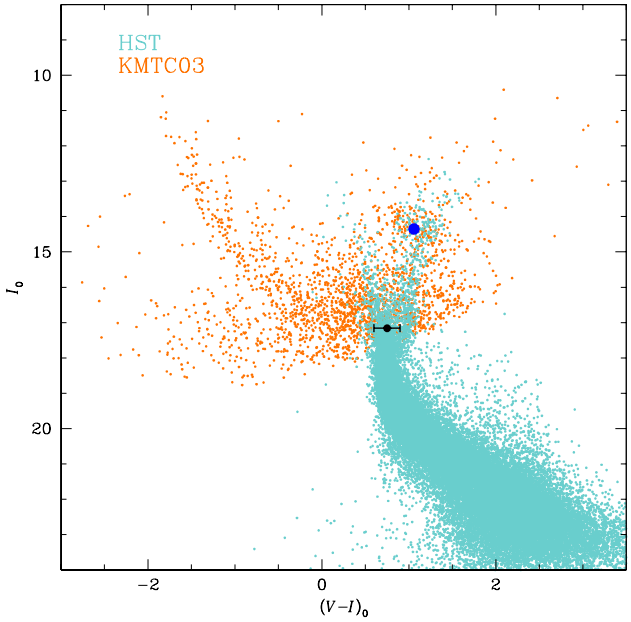

Figure 5. Color-magnitude diagram (CMD) of field stars in a 120″ square centered on the event OGLE-2017-BLG-1049. The blue and black dots indicate the positions of the Red Giant Clump centroid (RGC) and the source, respectively.

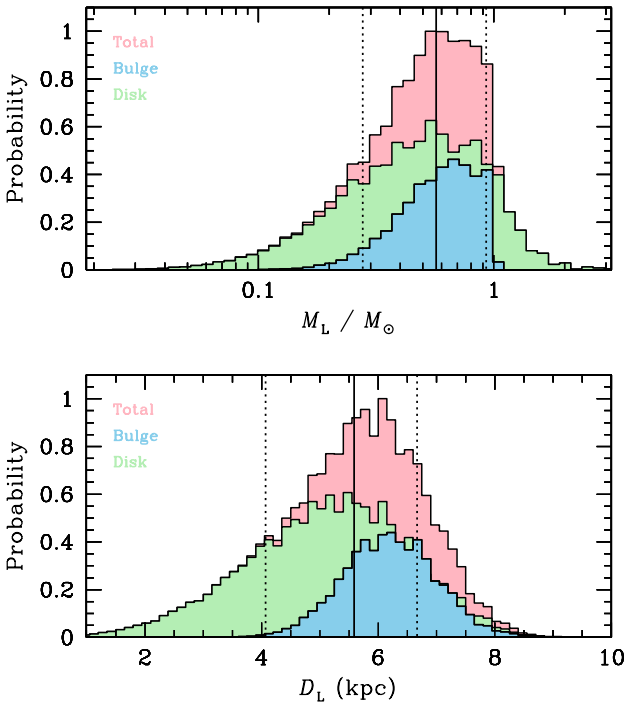

Figure 6. Probability distributions of the lens mass (host star) and distance to the lens derived from our Bayesian analysis. The vertical black solid line represents the median value, the two vertical dotted lines mark the 68% confidence interval.

they experience the same amount of extinction, resulting in

$$(V-I,I)_{\rm s,0} = (V-I,I)_{\rm s} - (V-I,I)_{\rm RGC} + (V-I,I)_{\rm RGC,0}. \quad (3)$$

However, the quality of KMTNet V-band data for this event was too poor to estimate a reliable color value; hence, we estimate the intrinsic V−I color $(V-I)_0$ using the Hubble Space Telescope CMD from Holtzman et al. (1998) following Section 5.2 of Bennett et al. (2008). The KMTNet CMD aligned to the HST CMD is shown in Figure 5. We adopt $(V-I,I)_{\rm RGC,0} = (1.06, 14.34)$ from Nataf et al. (2013). We find $(V-I,I)_{\rm s,0} = (0.75 \pm 0.15, 17.14 \pm 0.01)$. By using the VIK color-color relation from Bessell & Brett (1998) and the color-surface brightness relation from Kervella et al. (2004), we find that $\theta_* = 1.25 \pm 0.20$ μas. Note that the relation by Kervella et al. (2004) only applies to dwarf stars and subgiants. Judging by the color and source size, the source is likely a late G-type sub-giant star. The values for ρ and θ_* yield the angular Einstein radius of the lens system,

$$\theta_{\rm E} = \frac{\theta_*}{\rho} = 0.52 \pm 0.11 \ {\rm mas}. \quad (4)$$

Since the source is located in the region of the CMD where the giant branch separates from the main sequence, we repeat our calculations with a redder $(V-I)_{\rm s,0} = 1.0$ to check the impact of the color on the Bayesian fit. The difference in θ_* is less than 3%; therefore, we adopted $(V-I)_{\rm s,0} = 0.75$ which is the more likely value. The parameters related to the source star are summarized in Table 3.

4.2. Lens Properties

In order to determine the mass and distance of the lenses, measurements of the angular Einstein radius $\theta_{\rm E}$ and the microlens parallax $\pi_{\rm E}$ are required. This is because

$$M_{\rm L} = \frac{\theta_{\rm E}}{\kappa \pi_{\rm E}}, \quad D_{\rm L} = \frac{\rm au}{\pi_{\rm E}\theta_{\rm E} + \pi_{\rm S}}, \quad (5)$$

where $\kappa \equiv 4G/c^2 \backsimeq 8.144\,{\rm mas}\,M_\odot^{-1}$ and $\pi_{\rm S} = {\rm au}/D_{\rm S}$ is the source parallax (Gould 2000). Here we adopt $D_{\rm S} = 7.70$ kpc from Nataf et al. (2013). However, as mentioned above, there is no reliable parallax detection for OGLE-2017-BLG-1049. Hence, we perform a Bayesian analysis to determine $M_{\rm L}$ and $D_{\rm L}$, following the procedure described in Jung et al. (2018) except for the Galactic model, which is based on three priors of the velocity distribution, mass function, and matter density profile of the Galaxy. We use a new Galactic model based on more recent data and scientific understanding. The new Galactic model includes the disk density profile from a Robin-based Bennett model, the disk velocity dispersion (Bennett et al. 2014), and the bulge mean velocity and dispersions from *Gaia*, while the bulge density profile is the same as for the previous model (i.e., Jung et al. 2018). In the previous Galactic model, the bulge mean velocity was zero. With these three priors, we generate several tens of millions artificial microlensing events and investigate the probability distributions of $M_{\rm L}$ and $D_{\rm L}$ using the measured values of $t_{\rm E}$ and $\theta_{\rm E}$. We

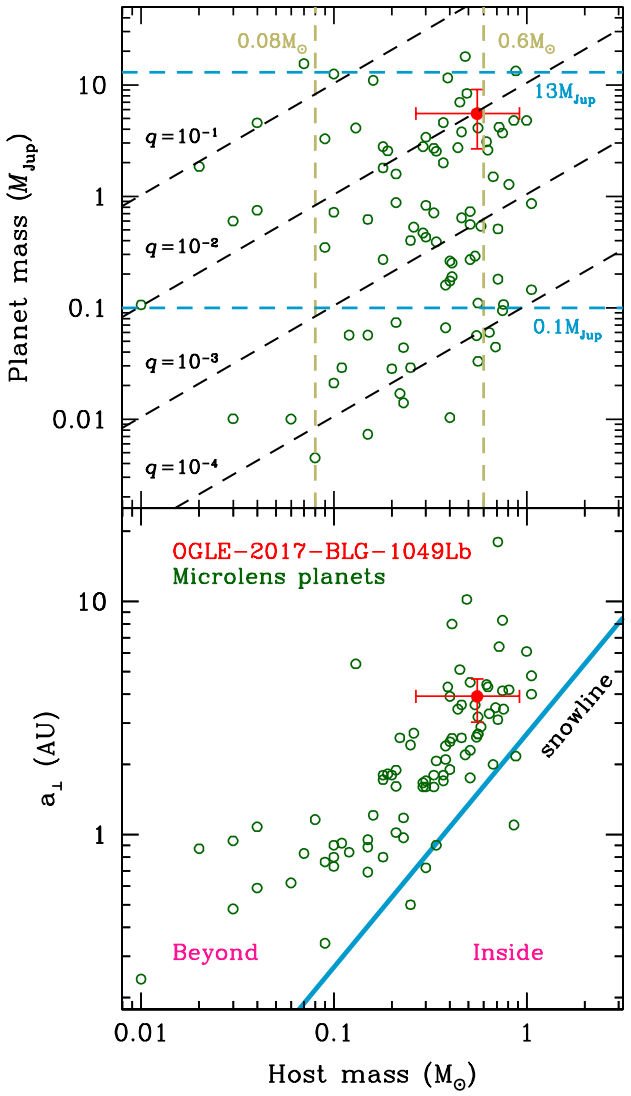

Figure 7. Distribution of microlensing exoplanets from the NASA exoplanet archive[1] in two different parameter planes. *Top panel:* The planet mass–host mass plane. The yellow vertical dashed lines indicate the mass limits of M dwarf stars (0.08–0.6$M_\odot$), the blue dashed lines mark the mass limits of giant planets (0.1–13$M_{\rm Jup}$). *Bottom panel*: The host star mass–projected semi-major axis plane. The diagonal blue line indicates the snow line $a_{\rm snow} = 2.7(M/M_\odot)$ au. In both panels, the red dot with error bars indicates the OGLE-2017-BLG-1049 planet.

find that the mass of and distance to the host star are

$$M_{\rm h} = 0.55^{+0.36}_{-0.29}\ M_\odot, \quad D_{\rm L} = 5.67^{+1.11}_{-1.52}\ {\rm kpc}, \qquad (6)$$

with the values being the median values of the probability distributions and the errors indicating the 68% confidence intervals (see Figure 6). We then estimate the mass $M_{\rm p}$ and the projected separation $a_\perp$ of the planetary companion, which are determined by $M_{\rm p} = qM_{\rm h}$ and $a_\perp = sD_{\rm L}\theta_{\rm E}$:

$$M_{\rm p} = 5.53^{+3.62}_{-2.87}\,M_{\rm Jup}, \quad a_\perp = 3.92^{+1.10}_{-1.32}\ {\rm au}. \qquad (7)$$

Table 1
Data sets and error rescaling parameters

Observatory (Band)	$N_{\rm data}$	k	σ_0 (mag)
OGLE (I)	235	1.450	0.002
KMTC BLG03 (I)	1238	1.189	0.000
KMTC BLG43 (I)	719	1.354	0.000
KMTS BLG03 (I)	1746	1.227	0.000
KMTS BLG43 (I)	1677	1.247	0.000
KMTA BLG03 (I)	1404	1.021	0.000
KMTA BLG43 (I)	1418	1.038	0.000
MOA (R)	3466	0.961	0.000

$N_{\rm data}$ is the number of data points. Parameter are defined in Equation (1).

Table 2
Best-fit parameters and their 68% uncertainty ranges from MCMC

Parameter	without MOA	**with MOA**
χ^2/dof	8335.887/8416	**11796.306/11880**
t_0 (HJD′)	7906.413 ± 0.029	$\mathbf{7906.453 \pm 0.027}$
u_0	0.180 ± 0.002	$\mathbf{0.183 \pm 0.002}$
$t_{\rm E}$ (days)	28.861 ± 0.283	$\mathbf{28.652 \pm 0.239}$
s	1.320 ± 0.003	$\mathbf{1.320 \pm 0.003}$
q (10^{-3})	9.645 ± 0.471	$\mathbf{9.534 \pm 0.386}$
α (rad)	0.474 ± 0.004	$\mathbf{0.478 \pm 0.003}$
ρ (10^{-3})	2.384 ± 0.052	$\mathbf{2.385 \pm 0.049}$
$f_{\rm s,OGLE}$	0.094 ± 0.001	$\mathbf{0.095 \pm 0.001}$
$f_{\rm b,OGLE}$	0.103 ± 0.001	$\mathbf{0.180 \pm 0.002}$

HJD′ = HJD−2450000 days. The values in bold face represent the adopted best-fit model.

Accordingly, the lens system of OGLE-2017-BLG-1049 is likely to be an M dwarf star hosting a super-Jupiter mass planet. Considering that the snow line of a host star scales as $a_{\rm snow} = 2.7(M/M_\odot)$ au (Kennedy & Kenyon 2008), the snow line of the lens system is located at $a_{\rm snow} \simeq 1.49$ au. This indicates that the planet lies beyond the snow line. All physical parameters of the lens found from the Bayesian analysis are listed in Table 4.

We additionally conduct a Bayesian analysis including additional parallax constraints. The nominal, best-fit value of the parallax is $\pi_{\rm E} \sim 4$, which implies $M_L \sim 0.015M_\odot$ and $D_L \sim 500$ pc. Such a result would be quite remarkable. However, the constraints on $\pi_{\rm E}$ are very weak (see Figure 4). Therefore, the Bayesian priors dominate over the parallax, and including the parallax hardly changes the results (Table 4).

Using the measured $\theta_{\rm E}$ and $t_{\rm E}$, we estimate the relative lens–source proper motion to be $\mu_{\rm rel} = \theta_{\rm E}/t_{\rm E} = 6.66 \pm 1.35\,{\rm mas\,yr^{-1}}$, which is a value consistent with disk objects. The Bayesian analysis supports a disk lens with $D_{\rm L} \sim 5.7$ kpc.

5. SUMMARY

We analyzed the planetary lensing event OGLE-2017-BLG-1049 with a short-timescale caustic crossing feature detected by KMTNet high-cadence observations. We adopted a best-fit model light curve including MOA data using a Bayesian analysis with the constraints

Table 3
Source parameters

Parameter	Values
$(V-I)_{\rm s,0}$	0.75 ± 0.15
$I_{\rm s,0}$	17.14 ± 0.01
θ_* (μas)	1.25 ± 0.20

Table 4
Lens parameters

Parameter	$t_{\rm E} + \theta_{\rm E}$	$t_{\rm E} + \theta_{\rm E} + \pi_{\rm E}$	
		$u_0 > 0$	$u_0 < 0$
$\theta_{\rm E}$ (mas)	$\mathbf{0.52 \pm 0.11}$	0.48 ± 0.10	0.49 ± 0.10
$\mu_{\rm rel}$ (mas/yr)	$\mathbf{6.66 \pm 1.35}$	5.97 ± 1.21	6.01 ± 1.21
$M_{\rm h}$ ($M_\odot$)	$\mathbf{0.55^{+0.36}_{-0.29}}$	$0.59^{+0.33}_{-0.26}$	$0.48^{+0.39}_{-0.27}$
$M_{\rm p}$ ($M_{\rm Jup}$)	$\mathbf{5.53^{+3.62}_{-2.87}}$	$7.70^{+4.33}_{-3.43}$	$5.90^{+4.80}_{-3.37}$
$D_{\rm L}$ (kpc)	$\mathbf{5.67^{+1.11}_{-1.52}}$	$6.09^{+0.95}_{-1.14}$	$5.54^{+1.25}_{-1.72}$
$a_\perp$ (au)	$\mathbf{3.92^{+1.10}_{-1.32}}$	$4.00^{+1.02}_{-1.10}$	$3.64^{+1.59}_{-1.06}$

$t_{\rm E}$, $\theta_{\rm E}$, and $\pi_{\rm E}$ are the constraints used in the Bayesian analysis. The values in bold face represent the preferred best-fit model.

$t_{\rm E} + \theta_{\rm E}$. From this, we found a star with mass $M_{\rm h} = 0.55^{+0.36}_{-0.29}\ M_\odot$ hosting a giant planet with a mass $M_{\rm p} = 5.53^{+3.62}_{-2.87}\ M_{\rm Jup}$. The projected star–planet separation is $a_\perp = 3.92^{+1.10}_{-1.32}$ au, indicating that the planet lies beyond the snow line. Thus, the lens system is likely to be an M dwarf star. However, it is also possible that the host star is a K or even G dwarf.

Figure 7 shows OGLE-2017-BLG-1049Lb compared to other known microlensing exoplanets. The uncertainties are the 1σ uncertainties derived from Bayesian analysis and are typical of such Bayesian mass estimates. The distributions suggest that the distribution of giant planets is uniform from M to G dwarfs, with no noticeable decline in the frequency of giant planets around M dwarfs. However, host mass measurements are necessary in order to disentangle the underlying population from the Bayesian priors.

In the case of OGLE-2017-BLG-1049, it should be possible to measure the flux from the host star in a few years from now. The source–lens relative proper motion is about $\mu_{\rm rel} \sim 7\ {\rm mas\,yr^{-1}}$, implying that, by 2026, the two stars will be separated by about 60 mas. Thus, the host star can probably be resolved by existing 10 meter class telescopes at that time, or (if necessary) by the extremely large telescopes currently under construction.

Acknowledgments

Work by Y. H. Kim was supported by the Korea Astronomy and Space Science Institute (KASI) grant 2020-1-830-08. This research has made use of the KMTNet system operated by KASI and the data were obtained at the three host sites CTIO in Chile, SAAO in South Africa, and SSO in Australia. The OGLE project has received funding from the National Science Centre, Poland, grant MAESTRO 2014/14/A/ST9/00121 to AU. The MOA project was supported by JSPS KAKENHI grant No. JSPS24253004, JSPS26247023, JSPS23340064, JSPS15H00781, JP17H02871, and JP16H06287. This work has made use of the NASA Exoplanet Archive, which is operated by the California Institute of Technology, under contract with the National Aeronautics and Space Administration under the Exoplanet Exploration Program. Work by CH was supported by the National Research Foundation of Korea (grants 2017R1A4A1015178 and 2019R1A2C2085965).

References

Albrow, M. D., Horne, K., Bramich, D. M., et al. 2009, MNRAS, Difference Imaging Photometry of Blended Gravitational Microlensing Events with a Numerical Kernel, 397, 2099

Alard, C., & Lupton, R. H. 1998, A Method for Optimal Image Subtraction, ApJ, 503, 325

Batista, V., Gould, A., Dieters, S., et al. 2011, MOA-2009-BLG-387Lb: A Massive Planet Orbiting an M Dwarf, A&A, 529, 102

Battacharya, A., Bennett, D. P., Anderson, J., et al. 2017, The Star Blended with the MOA-2008-BLG-310 Source Is Not the Exoplanet Host Star, AJ, 154, 59

Bennett, D. P., Bond, I. A., Udalski, A., et al. 2008, A Low-Mass Planet with a Possible Sub-Stellar-Mass Host in Microlensing Event MOA-2007-BLG-192, ApJ, 684, 663

Bennett, D. P., Batista, V., Bond, I. A., et al. 2014, MOA-2011-BLG-262Lb: A Sub-Earth-Mass Moon Orbiting a Gas Giant Primary or a High Velocity Planetary System in the Galactic Bulge, ApJ, 758, 155

Bennett, D. P., Bhattacharya, A., Beaulieu, J. -P., et al. 2019, Keck Observations Confirm a Super-Jupiter Planet Orbiting M Dwarf OGLE-2005-BLG-071L, AJ, 159, 68

Bessell, M. S., & Brett, J. M. 1988, JHKLM Photometry: Standard Systems, Passbands, and Intrinsic Colors, PASP, 100, 1134

Bond, I. A., et al. 2001, Real-Time Difference Imaging Analysis of MOA Galactic Bulge Observations During 2000, MNRAS, 327, 868

Boss, A. P., 2006, Rapid Formation of Gas Giant Planets around M Dwarf Stars, ApJ, 643, 501

Burrows, A., Hubbard, W. B., Lunine, J. I., & Liebert, J. 2001, The Theory of Brown Dwarfs and Extrasolar Giant Planets, RvMP, 73, 719

Chung, S.-J., Han, C., Park, B.-G., et al. 2005, Properties of Central Caustics in Planetary Microlensing, ApJ, 630, 535

Dominik, M. 1998, Galactic Microlensing with Rotating Binaries, A&A, 329, 361

Dong, S., Gould, A., Udalski, A., et al. 2009, OGLE-2005-BLG-071Lb, The Most Massive M Dwarf Planetary Companion?, ApJ, 695, 970

Erdl, H., & Schneider, P. 1993, Classification of the Multiple Deflection Two Point-Mass Gravitational Lens Models and Application of Catastrophe Theory in Lensing, A&A, 268, 453

Gaudi, B. S. 2012, Microlensing Surveys for Exoplanets, ARA&A, 50, 411

Gould, A. 1992, Extending the MACHO Search to Approximately $10^6 M_\odot$, ApJ, 392, 442

Gould, A. 1994, Proper Motions of MACHOs, ApJL, 421, 71

Gould, A., Miralda-Escude, J., Bahcall, & J. N. 1994, Microlensing Events: Thin Disk, Thick Disk, or Halo?, ApJ, 423, L105

Gould, A. 2000, A Natural Formalism for Microlensing, ApJ, 542, 785
Gould, A. 2001, Theory of Microlensing, ASPC, 239, 3
Gould, A., Udalski, A., An, D., et al. 2006, Microlens OGLE-2005-BLG-169 Implies That Cool Neptune-like Planets Are Common, ApJ, 644, 37
Han, C. 2005, Analysis of Microlensing Light Curves Induced by Multiple-Planet Systems, ApJ, 629, 1102
Han, C., Jung, Y. K., Udalski, A., et al. 2016, OGLE-2014-BLG-0257L: A Microlensing Brown Dwarf Orbiting a Low-mass M Dwarf, ApJ, 822, 75
Holtzman, J. A., Watson, A. M., Baum, W. A., et al. 1998, The Luminosity Function and Initial Mass Function in the Galactic Bulge, AJ, 115, 1946
Ida, S., & Lin, D. N. C. 2004, Toward a Deterministic Model of Planetary Formation. II. The Formation and Retention of Gas Giant Planets around Stars with a Range of Metallicities, ApJ, 616, 567
Jung, Y. K., Udalski, A., Gould, A., et al. 2018, OGLE-2017-BLG-1522: A Giant Planet around a Brown Dwarf Located in the Galactic Bulge, AJ, 155, 219
Kennedy, G. M., Kenyon, S. J., Bromley, B. C., et al. 2006, Planet Formation around Low-Mass Stars: The Moving Snow Line and Super-Earths, ApJ, 650, 139
Kennedy, G. M., & Kenyon, S. J. 2008, Planet Formation around Stars of Various Masses: The Snow Line and the Frequency of Giant Planets, ApJ, 673, 502
Kervella, P., Thévenin, F., Di Folco, E., & Ségransan, D. 2004, The Angular Sizes of Dwarf Stars and Subgiants. Surface Brightness Relations Calibrated by Interferometry, A&A, 426, 297
Kim, S.-L., Lee, C.-U., Park, B.-G., et al. 2016, KMTNET: A Network of 1.6 m Wide-Field Optical Telescopes Installed at Three Southern Observatories, JKAS, 49, 37
Kim, D.-J., Kim, H.-W., Hwang, K.-H., et al. 2018, Korea Microlensing Telescope Network Microlensing Events from 2015: Event-finding Algorithm, Vetting, and Photometry, AJ, 155, 76
Laughlin, G., Bodenheimer, P., & Adams, F. C. 2004, The Core Accretion Model Predicts Few Jovian-Mass Planets Orbiting Red Dwarfs, ApJL, 612, 73
Montet, B. T., Crepp, J. R., Johnson, J. A., et al. 2014, The TRENDS High-contrast Imaging Survey. IV. The Occurrence Rate of Giant Planets around M Dwarfs, ApJ, 781, 28
Nataf, D. M., Gould, A., Fouqué, P., et al. 2013, Reddening and Extinction toward the Galactic Bulge from OGLE-III: The Inner Milky Way's RV ~ 2.5 Extinction Curve, ApJ, 769, 88
Skowron, J., Udalski, A., Kozlowski, S., et al. 2016, Analysis of Photometric Uncertainties in the OGLE-IV Galactic Bulge Microlensing Survey Data, AcA, 66, 1
Skowron, J., Udalski, A., Gould, A., et al. 2011, Binary Microlensing Event OGLE-2009-BLG-020 Gives Verifiable Mass, Distance, and Orbit Predictions, ApJ, 738, 87
Sumi, T., Bennett, D. P., Bond, I. A., et al. 2010, A Cold Neptune-Mass Planet OGLE-2007-BLG-368Lb: Cold Neptunes Are Common, ApJ, 710, 1641
Sumi, T., Udalski, A., Bennett, D. P., et al. 2016, The First Neptune Analog or Super-Earth with a Neptune-like Orbit: MOA-2013-BLG-605Lb, ApJ, 825, 112
Udalski, A. 2003, The Optical Gravitational Lensing Experiment. Real Time Data Analysis Systems in the OGLE-III Survey, AcA, 53, 291
Udalski, A., Ryu, Y.-H., Sajadian, S., et al. 2018, OGLE-2017-BLG-1434Lb: Eighth $q < 1 \times 10^{-4}$ Mass-Ratio Microlens Planet Confirms Turnover in Planet Mass-Ratio Function, AcA, 68, 1
Vandorou, A., Bennett, D. P., Beaulieu, J.-P., et al. 2020, Revisiting MOA 2013-BLG-220L: A Solar-type Star with a Cold Super-Jupiter Companion, AJ, 160, 121
Yee, J. C., Shvartzvald, Y., Gal-Yam, A., et al. 2012, MOA-2011-BLG-293Lb: A Test of Pure Survey Microlensing Planet Detections, ApJ, 755, 102
Yoo, J., DePoy, D. L., Gal-Yam, A., et al. 2004, OGLE-2003-BLG-262: Finite-Source Effects from a Point-Mass Lens, ApJ, 603, 139